GEOPHYSICS, VOL. 72, NO. 2 (MARCH-APRIL 2007); P. G9–G20, 16 FIGS., 1 TABLE.
10.1190/1.2428267

Seismoelectric imaging of shallow targets

Seth S. Haines[1], Steven R. Pride[2], Simon L. Klemperer[3], and Biondo Biondi[3]

ABSTRACT

We have undertaken a series of controlled field experiments to develop seismoelectric experimental methods for near-surface applications and to improve our understanding of seismoelectric phenomena. In a set of off-line geometry surveys (source separated from the receiver line), we place seismic sources and electrode array receivers on opposite sides of a man-made target (two sand-filled trenches) to record separately two previously documented seismoelectric modes: (1) the electromagnetic interface response signal created at the target and (2) the coseismic electric fields located within a compressional seismic wave. With the seismic source point in the center of a linear electrode array, we identify the previously undocumented seismoelectric direct field, and the Lorentz field of the metal hammer plate moving in the earth's magnetic field. We place the seismic source in the center of a circular array of electrodes (radial and circumferential orientations) to analyze the source-related direct and Lorentz fields and to establish that these fields can be understood in terms of simple analytical models. Using an off-line geometry, we create a multifold, 2D image of our trenches as dipping layers, and we also produce a complementary synthetic image through numerical modeling. These images demonstrate that off-line geometry (e.g., crosswell) surveys offer a particularly promising application of the seismoelectric method because they effectively separate the interface response signal from the (generally much stronger) coseismic and source-related fields.

INTRODUCTION

The diversity and resolution of information that can be gained from geophysical studies are generally exceeded by the expectations and needs of those who use the information. In particular, geophysical surveys are limited in their ability to adequately characterize pore fluid and permeability heterogeneities, often leading to large uncertainties in fluid-flow models and contamination assessments. Electrokinetic phenomena represent the interrelation between mechanical energy, fluid flow, and electrical energy. Seismoelectric imaging can combine the high spatial resolution of seismic data with the sensitivity of electrical methods to fluid content, connectivity, and composition. These phenomena fall into two categories: electric-to-seismic conversions and seismic-to-electric conversions. This paper deals with seismic-to-electric conversions, which we refer to as *seismoelectric*, reserving the term *electroseismic* for the electric-to-seismic conversions, although this distinction has not been observed uniformly in previous literature (e.g., Haines et al., 2003).

A compressional wave traveling through a fluid-saturated porous material creates a fluid pressure gradient and an acceleration of the grain matrix, both of which induce pore-fluid flow. Because of the electric double layer (e.g., Shaw, 1992) that exists at the grain-fluid boundary, the pore-fluid movement transports a small (but consequential) amount of electric charge relative to the fixed charge on the adjacent grains (Figure 1a). The strength and polarity of the electric double layer varies with grain composition and fluid chemistry, but often (such as for quartz grains) the grain-surface charge is negative and the fluid positive. The net flow of charge relative to the grains is a streaming electric current that creates a charge separation within a compressional wave at the scale of the seismic wavelet. This charge separation has an associated electric field, which we refer to as the *coseismic* field, colocated with a compressional (P-) wave (Pride, 1994) (Figure 1a). This is the most commonly and readily observed seismoelectric phenomenon (e.g., Ivanov, 1939; Garambois and Dietrich, 2001). In the case of partial water saturation, water still coats the grain surfaces, and wave-induced acceleration of the grain framework is the dominant force, causing relative grain/fluid flow and thus creating electric fields. All seismoelectric fields discussed in this paper can be generated under the condition of partial water saturation.

Manuscript received by the Editor January 12, 2005; revised manuscript received September 13, 2006; published online January 30, 2007.
[1]Formerly Stanford University, Department of Geophysics, Stanford, California; presently U. S. Geological Survey, Crustal Imaging and Characterization Team, Denver, Colorado. E-mail: shaines@usgs.gov.
[2]Lawrence Berkeley National Laboratory, Earth Sciences Division, Berkeley, California. E-mail: srpride@lbl.gov.
[3]Stanford University, Department of Geophysics, Stanford, California. E-mail: sklemp@stanford.edu; biondo@sep.stanford.edu.

The second recognized seismoelectric phenomenon occurs when a P-wave encounters an interface in material properties (elastic, chemical, flow related, etc). The charge separation in the wave is disturbed (Figure 1b), causing asymmetry in the charge distribution and resulting in what can be approximated as an oscillating electric dipole, with its dominant contribution coming from the first seismic Fresnel zone (Thompson and Gist, 1993; Haartsen and Pride, 1997). A significant portion of the first Fresnel zone acts as a disk of electric dipoles oriented normal to the interface. This disk of dipoles oscillates with the waveform of the seismic wave. But because the electromagnetic (EM) skin depth at seismic frequencies is typically much larger (≥ 1 km) than the offsets of interest in a shallow survey, the electric fields generated at the interface can be modeled as being created by a quasi-static dipole (e.g., Garambois and Dietrich, 2001). In our frequency band of interest (~ 10 Hz to 1 kHz), we are within the near-field diffusive regime and thus do not need to consider attenuation of the electromagnetic signals. The electric field of this EM disturbance (Figure 1b), called the *interface response*, can be measured almost immediately at the earth's surface (e.g., Martner and Sparks, 1959; Butler et al., 1996) because the EM traveltime is negligible compared with the seismic traveltime ($V_{EM} \approx 10^3$ to $10^5 V_P$). The interface response is created at heterogeneities that can otherwise be difficult to image, such as flow-property variations and spatial changes of pore-fluid chemical properties such as pH and salinity (Haartsen and Pride, 1997; Garambois and Dietrich, 2002).

A third type of seismoelectric phenomenon is predicted by Pride and Haartsen (1996) and was first reported by Haines et al. (2004). We term this the *direct field*, because it can be thought of as analogous to the seismic direct wave. A directed point source (e.g., a sledgehammer impact, as opposed to an isotropic explosion) creates relatively enhanced fluid pressure on one side of the impact point (beneath the hammer strike plate). The fluid-pressure distribution equilibrates, resulting in an electrokinetically induced charge separation. The charge separation at a vertical impact point will have a strong vertical dipole component. The associated electric field emanating from the region of impact is what we call the *direct field* (Figure 1c). Similar to the interface response, the direct field shows the amplitude pattern of a dipole and reversed polarity on opposite sides of the shotpoint. It occurs at the time of the source impulse and continues until the region of the impact point has relaxed to its original state.

If the source is a mass impacting a metal plate, seismoelectric data may contain a similar-looking, but entirely unrelated, electric field. This is the field **E** created by moving a conductor (the metal plate) with velocity **v** within the earth's magnetic field **B**, described by the Lorentz equation $\mathbf{E} = \mathbf{v} \times \mathbf{B}$. We refer to this field as the *Lorentz field*.

Most of the published seismoelectric data can be considered observations of phenomena rather than applications of the method to a particular geophysical problem. A key distinction can be made between the analysis of unstacked shot gathers corresponding with a 1D region of the subsurface and interpretable (2D or 3D) images made up of stacked shot gathers. Because the interface response is created at only one location per interface per seismic source point (in contrast to seismic reflections), seismoelectric shot gathers may be stacked to collapse the interface response energy in the shot gather to a single trace that can then be used as part of an image. Thompson and Gist (1993) were the first to present a seismoelectric image of the subsurface, produced by processing and stacking one hundred 52-channel shot gathers collected over stratified sediments in an oil and gas field. Their image shows arrivals interpreted as the interface response from thin layers in the upper 100 m and from layers as deep as 300 m. Thompson et al. (2005) present 3D reservoir images created with the (distinct but related) electroseismic method, demonstrating the method's sensitivity to pore-fluid composition.

Along with advances in field methods has come the development of numerical modeling techniques to simulate seismoelectric phenomena. Haartsen and Pride (1997) and Garambois and Dietrich (2002) describe similar methods for modeling seismoelectric phenomena in layered media. Numerical simulation of laboratory (Zhu et al., 2000) and field (Mikhailov et al., 1997) shot gathers represents important progress toward fully understanding observed seismoelectric phenomena. Haines and Pride (2006) describe an algorithm for numerical simulation of seismoelectric phenomena with full 2D or 3D heterogeneity, providing a means for simulating seismoelectric images of complex targets.

Our study focuses on applying the seismoelectric method to near-surface geophysical problems. Our purpose is to establish how the method can best be used and to which applications it is best suited. The objective is to isolate the different types of seismoelectric fields so we can analyze them. Seismoelectric data, when collected with a geometry similar to conventional surface seismic data, comprise the interface response from subsurface layers and coseismic and direct fields, all of which can overlap in shot gathers. Because the interface response field (essentially

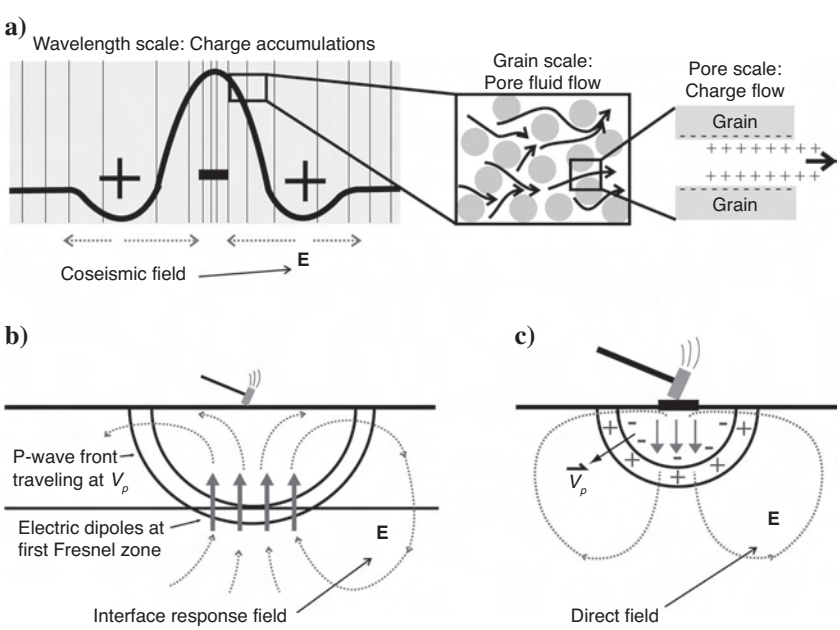

Figure 1. (a) The coseismic field is an electric field in a P-wave caused by charge accumulations that result from streaming currents. (b) The interface response is the electric field of an asymmetrical charge distribution that occurs when the streaming currents are disrupted by a change in mechanical or chemical properties. (c) The seismoelectric direct field is the electric field of the asymmetric charge distribution at an impact source.

that of a dipole) falls off as the distance cubed, the response from layers at depth can be orders of magnitude weaker than the coseismic fields. We employ unique experimental geometries to separate and study the seismoelectric fields. By placing sources and receivers on opposite sides of a man-made vertical interface (two parallel, sand-filled trenches), we record the interface response separately from the coseismic fields. With data interpretation facilitated by the known target, we are able to analyze the seismoelectric arrivals and compare data-acquisition procedures. In other experiments, we use linear and circular electrode arrays to study the source-related fields in detail. We use our findings to design an experiment to image a man-made target composed of two sand-filled trenches. Our image is matched by a synthetic image numerically modeled with the algorithm described by Haines and Pride (2006). Created with sources and receivers separated and on opposite sides of the target, our image demonstrates the value of using such geometries (e.g., crosswell surveying) to separate the weak interface response signal from the strong coseismic energy.

FIELD EXPERIMENTATION

Field sites

We have recorded seismoelectric data at two different field sites in the San Francisco Bay area. Our primary site is a small meadow at the Pride Mountain Vineyards on the ridge between Napa and Sonoma Valleys in St. Helena, California. The subsurface geology consists of clay-rich soil to a depth of at least 3 m, based on seismic surveys and excavation; highly weathered volcanic bedrock is suspected to lie at a depth of >10 m. The water table is close to 100 m deep; however, the soils contain greater than 50% water saturation (measured in August, during the dry season). During the winter and spring, after receiving >1 m of rainfall, saturation is closer to 100%. In this meadow, we constructed two trenches, approximately ~ 0.6 m wide, ~ 2.5 m deep, and 18 m long. The trenches are 2 m apart and are filled with sand (Figure 2).

We also conducted experiments at the Thompson redwood tree farm in the Santa Cruz Mountains on the San Francisco Peninsula in a small, level clearing with clayey soil. Seismic and geologic data suggest that bedrock is a few meters deep and that the uppermost several meters of bedrock are highly weathered (G. Thompson, personal communication, 2001). We used this site to test basic field methodologies and to study site-related variables.

Data acquisition

We collect seismoelectric data using a standard engineering seismograph—in our case, a Geometrics 24-channel Geode, sometimes augmented with a second 24-channel Geode. Each channel of the seismograph records the voltage difference across a pair of grounded electrodes (essentially acting as a 24-or 48-channel voltmeter). Our electrodes are 0.95-cm-diameter stainless steel rods that are ~ 0.9 m long with sharpened tips, pounded almost completely into the ground. We typically use a spacing of about 1 m between the two electrodes in a given pair and overlap electrode pairs if necessary to achieve station spacing smaller than dipole width. We improve electrode coupling by thoroughly wetting the soil around the electrodes with water and have found that the addition of salt or other conductive agents does not result in appreciable improvement. The impedance across a pair of electrodes must be several orders of magnitude less than the input impedance of the seismograph (typically 20 kΩ) for proper instrument performance and optimal data quality. To eliminate the resonant electrical noise caused by the lightning-protection circuitry in the seismograph, we isolate each channel of the instrument from the electrodes with a 5:1 step-up transformer. This also provides a stronger signal to the recording instrument, a benefit as we try to record signals that are close to the seismograph sensitivity level. Preamplifiers (e.g., Butler et al., 2002) would fulfill both of these objectives and also provide the desired low impedance to the seismograph, but at greater cost. We find that grounding the seismograph (attaching a wire from the grounding jack on the seismograph to a dedicated electrode) helps to maintain data consistency and avoids spurious instrument-related noise.

The layout of the vineyard field site provides a great deal of versatility in recording geometry. We can place sources and receivers on opposite sides of the trenches, simulating a crosswell geometry (off-line geometry source point, Figure 2). The seismic wave encounters the interface and creates the interface response before the seismic wave (and associated coseismic field) reaches the receiver electrodes. To simulate a typical surface survey of subsurface targets (the geometry generally used in surface seismic surveys, Figure 1b), we also collect data with the source located within the receiver line (on-line source point, Figure 2). In this case, the coseismic energy and interface response are recorded simultaneously at near offsets and are temporally separated only at far offsets. We also used a recording geometry with the seismic source in the center of a circular electrode array to analyze source-related fields. In addition, we conducted on-line geometry surveys about 20 m from the trenches to study source-related fields in the absence of trench-related signals.

We generally record 1-s records at a sample rate of 4000 Hz, including a half-second of pretrigger recording for noise estimation. Typical signal measurements are on the order of 0.1 mV for the coseismic energy and 0.001 mV for the interface response in stacked records. Noise levels are typically ~ 0.01 mV for noise from the electric power grid (at 60 Hz and its harmonics) and ~ 0.001 mV for other background electrical noise at our vineyard field site. At the tree farm site, we find 60-Hz noise levels of about 0.001 mV and background electrical noise at about 0.0002 mV for stacked records. At our sites, we do not find any evidence of data contamination by AM radio broadcasts, a problem encountered using similar instrumentation at other sites (K. Butler, personal communication, 2003).

Many additional experiments documenting the effects of variations on the data acquisition methodology are described by Haines (2004). We briefly summarize those findings. First, the electrode spacing cause cancelation of frequencies of the coseismic field that have a wavelength that is an integer multiple of the width of the elec-

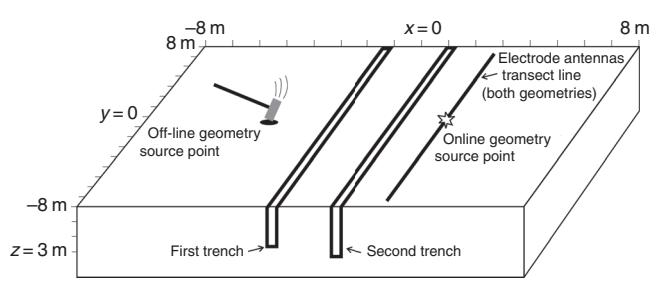

Figure 2. Layout of vineyard field site, showing two of the several recording geometries that we used: the off-line geometry with the source points opposite the electrodes and the online geometry with the source points within the electrode array.

trode pairs. The interface response has a very high apparent velocity, so it is not affected. Second, based on a comparison between data collected with and without geophones present within the electrode line, geophones positioned within electrode pairs do not have any effect on the recorded seismoelectric signal (any field created by the moving geophone is significantly weaker than the fields of interest and does not appear in our field data), so we can collect seismic and seismoelectric data simultaneously without signal contamination. Third, simple experiments using electrode receiver groups (electrode pairs wired together to cancel coseismic surface-wave energy) were unsuccessful, though this topic may warrant further experimentation. Finally, 24 recording channels is adequate, but a greater number is preferable for better identification of weaker and more complicated signals.

Seismic sources

We have collected well over 300 seismoelectric shot gathers, the vast majority of which have been the result of stacked hammer impacts (generally 25–50 impacts of a 5.4-kg sledgehammer per shot gather). The hammer is struck on a hammer plate partially embedded in the soil. We trigger the seismograph with a standard mechanical (contact closure) hammer switch. Because of the time-variable nature of electrical noise, we prefer to record the impacts individually, manually remove those that show excess electrical noise, and then stack the remaining records to produce a single shot gather. We have tested various hammer plate options and find we get the best results when we use an 8.5-kg aluminum cylinder of 7 cm radius and 20 cm in length or a 3.4-kg polycarbonate plastic plate measuring 31 cm $\times$ 17 cm $\times$ 5 cm thick. The aluminum cylinder is placed with the axis horizontal and is struck on the side such that the rounded surface tends to equalize irregular hammer strikes. We also find that softer materials such as aluminum result in greater strike-to-strike repeatability than stiffer materials (e.g., steel), probably because the softer materials absorb a small amount of energy with plastic deformation, and further equalizing irregular impacts. However, like all metal plates, the cylinder can create the Lorentz electric field. The plastic plate avoids the Lorentz field, with a very slight decrease in strike-to-strike repeatability. An example hammer-source seismoelectric shot gather is shown in Figure 3a. The 24 channels of electrodes (1.05-m dipoles at a spacing of 0.7 m) were located 2 m from the second trench, with the source located in the center of this array (online source point). These, and all data in this paper, are displayed using grayscale plots to preserve the broad dynamic range of seismoelectric data without compromising the waveforms of the arrivals. All data are displayed after removing power-line harmonic noise using the sinusoidal subtraction technique described by Butler and Russel (1993), unless otherwise noted.

We tested a Betsy seisgun firing blank 400-grain, 8-gauge shells. The seismograph was triggered using a contact-closure mechanism between the gun itself and the small hammer used to fire it. We found it essential to insulate the gun from the trigger circuitry to avoid large electric fields created when the trigger circuit closed. For the seisgun gather shown in Figure 3b, the gun was angled about 50° from vertical, toward the trenches, to direct more energy to the trenches. These data were acquired on the same day as the sledgehammer data and with the same geometry. We see that the stacked hammer strikes (Figure 3a) produce greater energy and a better signal-to-noise ratio (SNR) than the seisgun.

We conducted a series of experiments with chemical explosives at the vineyard site using a variety of online and off-line geometries. The gather shown in Figure 3c was collected using a 0.15-kg explosive charge buried 1.5 m deep at about 1 m from the receiver electrodes, which were 2 m from the second trench (so the shot was $\sim$3 m from the nearest trench). For this shot gather, power-line noise was removed using the methods described by Butler and Russel (2003). We interpret the strong flat energy in the upper 15 ms as direct-field energy, present even though explosives are not an impact source. This field is created because an explosive detonated in a shallow hole is not truly isotropic; unless the shot hole is perfectly backfilled, energy propagates preferentially upward to the free surface and creates an asymmetrical pressure (and charge) distribution that is essentially the same as the direct field observed with hammer impacts. Displays of the same data that include the full frequency bandwidth show the flat energy as basically one event, as is expected for an upward surge of energy followed by the relaxation of the earth to its original state.

Haines (2004) provides full details and data plots for all of these seismic sources as well as for an in-house vibrator source (Haines, 2006) that produced too much electrical noise to be useful. As with seismic work (e.g., Miller et al., 1992, 1994), we must assume that these findings are site specific and will not hold at all locations.

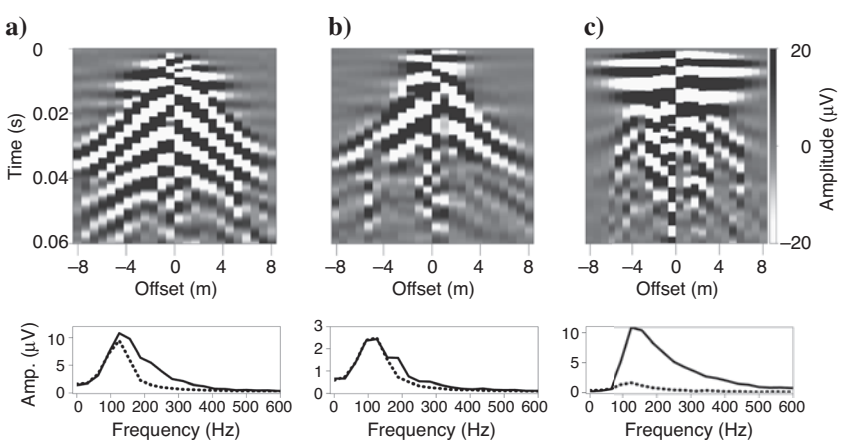

Figure 3. In-line geometry seismoelectric data recorded with the electrode array positioned 2 m from the second trench and with various seismic sources: (a) sledgehammer, (b) seisgun, and (c) explosive. Data are shown after 120–300-Hz band-pass filtering. Mean (all traces) true-amplitude spectra are computed after broadly tapered 120-Hz low-cut filtering to more clearly portray the spectra in the frequency band of interest (otherwise, strong, low-frequency energy would dominate the plots). The solid line is for the 0.0–0.02-s window, and the dashed line is for the 0.02–0.04 s window.

SOURCE-RELATED ELECTRIC FIELDS

Observing the direct and Lorentz fields

To develop our understanding of the source-related electric fields that may be observed in seismoelectric data, we begin with the simplest possible data-collection scenario and add complexity one step at-a-time. In this way, we can better identify the effect of each individual element of seismoelectric data collection.

The gathers shown in Figure 4 were collected at the vineyard field site but far away (~20 m) from the trenches, which are therefore thought to have no effect on the data. The data were collected with a source point in the center of a linear array of 24 electrode pairs deployed with of 0.7 m spacing between the centers of adjacent pairs. The distance across each pair of electrodes (the dipole width) was 1.05 m. We first confirmed that the trigger mechanism produces no electrical noise by collecting data by simply hitting the trigger switch against a stationary object (the handle of a sledgehammer held off the ground). These data show only the background electrical noise.

We add a level of complexity by putting seismic energy into the ground, but with no moving metal objects. Figure 4a shows data collected using the impact of a wooden source (a fence post) on the plastic hammer plate. We see the expected dipping coseismic energy (with seismic moveout), labeled CS. We also observe flat (no moveout) energy in the upper approximately 17 ms of the record, labeled D. This energy appears to show the amplitude pattern of a dipole and reversed polarity on opposite sides of the shotpoint. If we had reason to believe that the site geology included any sufficiently shallow interfaces (in the upper ~2 m), we would conclude that this flat energy was the seismoelectric interface response. Because we are not aware of any shallow interfaces (based on trenching to 3 m depth), we interpret this energy as the seismoelectric direct field.

We add another level of complexity by using a metal sledgehammer on the plastic hammer plate and observe that the result is very similar to that of Figure 4a. We can conclude that the moving metal hammerhead does not create a noticeable electric field. We move one step further by using a metal hammer plate (the aluminum cylinder). We now observe (Figure 4b) an additional form of flat energy in the upper approximately 10 ms of the record, labeled L. It shows no moveout and has an amplitude pattern suggestive of a dipole. But unlike the interface response and the direct field, this energy shows the same polarity on the two sides of the shotpoint. We conclude that this field is caused by a horizontal electric dipole oriented along the electrode transect line, created by the Lorentz field of the moving metal hammer plate. Though both the direct and Lorentz fields are EM disturbances created at the seismic source point, the direct field is observed at a slightly later time because its creation is delayed by the time required for the soil to respond to the hammer impact.

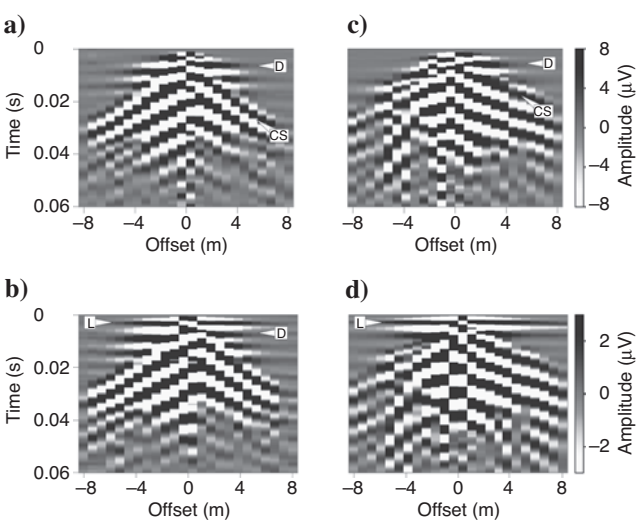

Figure 4. Seismoelectric shot gathers collected at the vineyard and tree farm field sites, testing impact source options. (a) Data from the wooden fence post on the plastic hammer plate at the vineyard site show flat direct field arrivals (D) and dipping coseismic energy (CS). (b) The metal sledge on the aluminum hammer plate at the vineyard site shows the addition of flat Lorentz field energy in the upper 0.01 s (L). (c) The wooden source on the plastic plate and (d) the metal sledge on the aluminum plate, both at the tree farm site, show very similar patterns to (a) and (b), though the direct field arrival is weaker and is almost entirely obscured by the Lorentz field in (d).

We gain more certainty in our interpretations by looking at comparable data collected at the tree farm field site (Figure 4c and d) and observe exactly the same patterns in those data. The wooden source on the plastic plate (Figure 4c) produces the direct field D, and the hammer on the aluminum source (Figure 4d) produces the direct field D along with the Lorentz field L. The fact that the data from the two sites are so similar, despite the dissimilarities of the sites, suggests that the underlying physics is the same and that this flat, polarity-reversed energy must be the direct field.

Seismoelectric direct field

To characterize the direct and Lorentz fields, we conducted a series of experiments with various sources in the center of a circular electrode array (Figure 5). The electrode pairs were spaced evenly around a circle of 4.3 m radius in a homogeneous part of the vineyard meadow, with 12 electrode pairs oriented radially and 12 oriented tangentially. Thus, tangential and radial pairs of electrodes were colocated at 30° intervals around the circle. The electrodes were wired such that radial fields would show the same polarity on all radial electrode pairs and any fields oriented circumferentially would show the same polarity on all tangential electrode pairs. We also collected data with horizontal geophones deployed in the same geometry (radial and tangential phones at 30° intervals around the circle). The source point was in the center of the circle for all shot gathers.

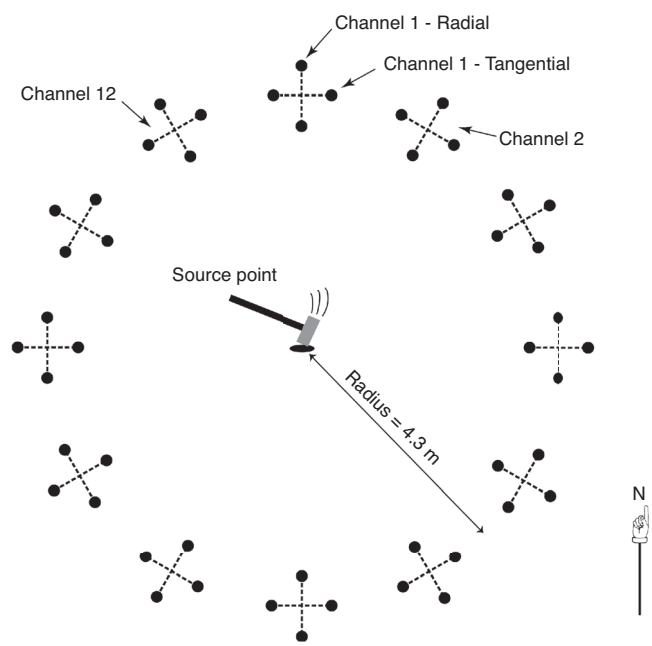

Figure 5. Circular electrode array with 12 radial and 12 tangential channels. Small black circles represent electrodes, and dashed lines indicate the pairs across which we measure voltages.

Figure 6a shows the radial traces of a seismoelectric shot gather collected with 25 sledgehammer impacts on the plastic plate. Based on arrival times from Figure 4a, the strong coherent arrival at 0.02 s is the coseismic energy, and the weaker arrival at 0.01 s is the direct field. These arrivals do not appear in the tangential part of the same shot gather (Figure 6b), as is to be expected for a vertical dipole (the direct field) and radially propagating seismic energy (the coseismic arrival). Further confirmation of our interpretation of the 0.02-s arrival as coseismic energy is provided by the corresponding radial horizontal geophone data shown in Figure 6c, where we see that the first seismic arrival closely matches the interpreted coseismic arrival in Figure 6a. The lack of any energy at ~ 0.01 s in Figure 6c supports our interpretation of the 0.01-s energy in Figure 6a as the direct field, or at least as a seismoelectric arrival. As expected, the tangential geophone data (Figure 6d) do not show coherent arrivals.

The direct field energy in Figure 6a shows (approximately) constant amplitudes around the circle, consistent with the interpretation that this energy is caused by a vertical dipole. We can constrain the size and location of this dipole by considering the amplitude pattern of the online shot record in Figure 4a. Figure 7a shows the same data but with a broader band-pass filter (20–800 Hz) so as to better represent the full direct field, which can be clearly seen as a single strong arrival at about 0.005 s. The amplitude of the maximum of this arrival is plotted as dots in Figure 7b. Using the simple equation for the potential field of a quasi-static current dipole (e.g., Landau and Lifshitz, 1984),

$$\Phi(x,z) = \frac{I}{2\pi\sigma}\,\frac{z}{(x^2+z^2)^{3/2}}, \tag{1}$$

we model the amplitude pattern that we expect for a dipole at a given location. Here, I is the magnitude of the seismically induced streaming current, located at a depth z from the surface. We observe the field from a position along the receiver line that is offset from the dipole by a distance x and assume that the earth is homogeneous and has an electrical conductivity σ.

We model amplitudes corresponding with a disk of dipoles with 0.8 m radius and located at a lateral distance (depth) of 0.8 m. The absolute magnitude of the modeled current dipole is arbitrary; we scale I/σ in equation 1 to match the field data. We approximate the disk of dipoles (following Garambois and Dietrich, 2001) by summing the contributions of 100 dipoles spread along the a disk of 0.8 m radius. The modeled amplitude pattern is plotted as a solid line in Figure 7b. The fit of this model to the data broadly indicates that the direct field is produced within a soil volume of approximately 0.8 m radius.

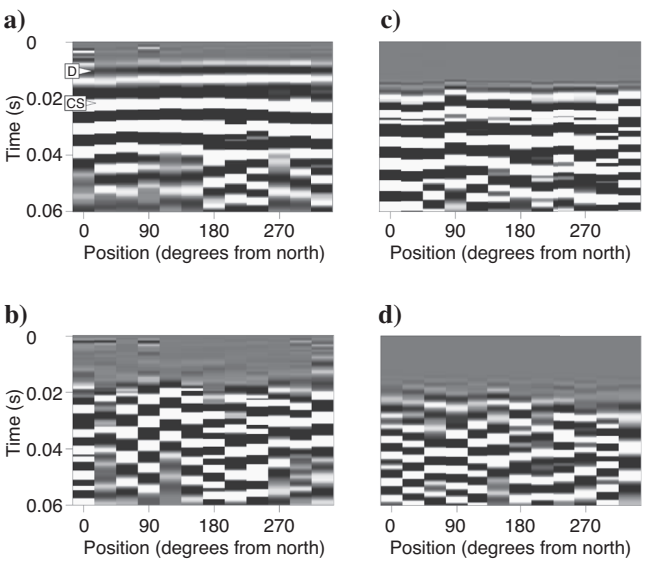

Figure 6. Stacked shot gathers recorded by the circular electrode array. (a) The radial component of the electric field created by the impact of a sledgehammer on a plastic plate shows the coherent direct field arrival at about 0.01 s (D) and higher-amplitude coseismic arrival at around 0.02 s (CS). (b) The tangential component of the same shot gather (hammer on plastic plate) shows no coherent arrivals. (c) The radial component of horizontal geophone data shows the first seismic arrival at approximately 0.02 s, corresponding with coseismic arrival in (a). (d) The tangential component of geophone data shows no clear coherent arrivals.

Lorentz field of the metal hammer plate

An important observation about the Lorentz field is that its polarity can change from one hammer strike to the next, such that for a set of hammer impacts on the aluminum cylinder, approximately half of the raw gathers show a Lorentz field with one polarity and the other half show the opposite polarity. The stack in Figure 4b is composed of shot gathers selected on the basis of the polarity of the Lorentz field. The other gathers collected at this source point produce a stack with a Lorentz field arrival with opposite polarity. A stack of all of the shot gathers shows very little Lorentz energy, as it tends to stack out. Data collected when we intentionally strike the plate or cylinder in a particular horizontal direction show no strike-to-strike reversals.

This polarity reversal leads us to the somewhat surprising conclusion that the field is created by the horizontal motion of the cylinder **v** crossed with the vertical component of the earth's magnetic field **B**, as shown in Figure 8. The horizontal component of **v** can reverse between sequential hammer strikes, while **B** is constant (oriented toward magnetic south at an angle $\sim 60°$ from horizontal). After the first few hammer impacts compact the soil beneath the hammer plate (or cylinder, in this experiment), it has more freedom to move horizontally than vertically. So although the impact is almost entirely vertical, even a small deviation (nonvertical strike or off-center impact on the rounded top surface of the cylinder) can produce a briefly high horizontal velocity **v**. For our data, the aluminum cylinder was

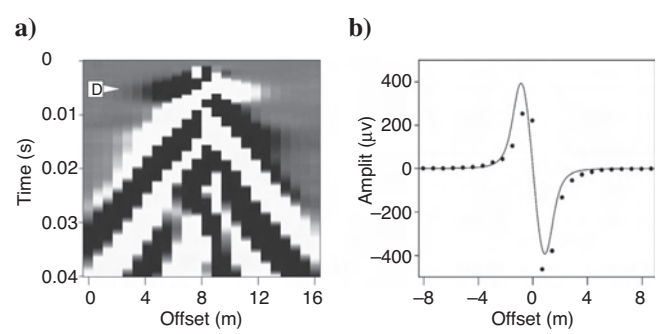

Figure 7. Direct field amplitudes. (a) The shot gather from Figure 4a with a band-pass filter of 20–800 Hz shows strong, direct-field energy (D). (b) The amplitude pattern for the direct field arrival is plotted as dots, and modeled amplitudes are as a solid line. Modeled amplitudes correspond with a disk of electric dipoles of 0.8 m radius centered 0.8 m away from the electrode array.

oriented along the electrode receiver line: thus, the hammer strikes tended to cause horizontal motion perpendicular to the line.

Data collected by the circular electrode array using the sledgehammer on the aluminum cylinder are shown in Figure 9. Figure 9a and b are the radial and tangential parts of a stack of those hammer strikes that show one polarity of the interpreted Lorentz field energy, and Figure 9c and d are the radial and tangential parts of a stack of the other hammer strikes, which show opposite polarity. These two sets of impacts were selected from the individual hammer-strike gathers based on the presence and polarity of the events that appear between approximately 0.001 and 0.007 s at certain radial positions (90°–180° and 270°–360°) in the radial component and 90° out-of-phase (0°–90° and 180°–270°) in the tangential component. We interpret these arrivals as the Lorentz field; note their polarity is reversed between the two stacks (Figure 9a and b, versus Figure 9c and d). The direct field arrivals (D) show amplitude variation around the circular electrode array because of interference with the Lorentz field.

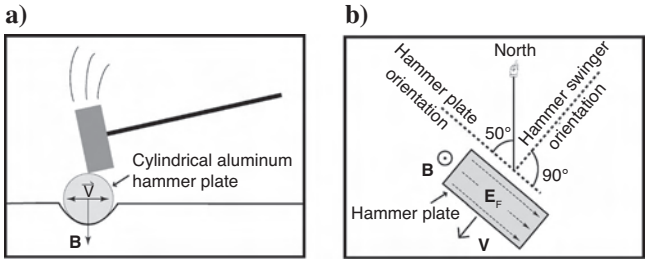

Figure 8. (a) Side and (b) map views of the creation of the Lorentz field. The horizontal component v_h of the hammer plate velocity **v** crossed with the vertical component of the earth's magnetic field **B** creates an electric field **E** in the conductive the plate. The value v_h varies from strike to strike and may be in either direction.

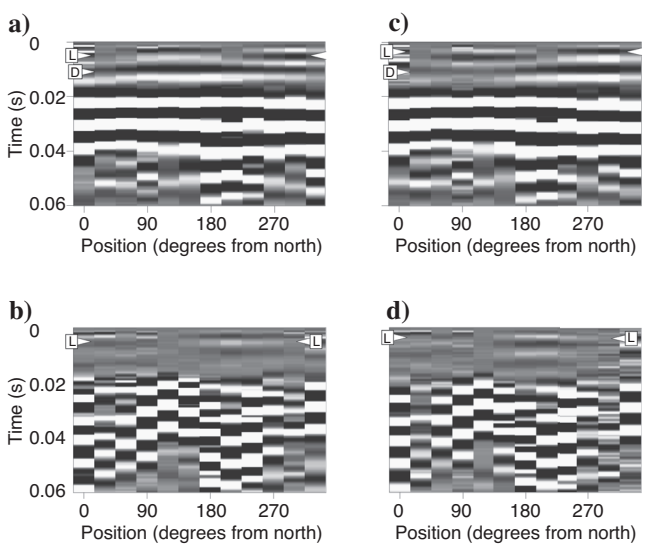

Figure 9. Seismoelectric data collected with a sledgehammer on the aluminum cylinder and recorded by the circular electrode array. Lorentz energy (L) can be seen near 0.001 s, above the direct field (D) in each gather. (a) The radial component of a stack of selected hammer strikes shows Lorentz energy near 0.001s at 90°–180° and 270°–360°. (b) The tangential component of the same stacked gathers shows faint Lorentz energy near 0.001 s at positions orthogonal to the energy in (a). (c) The radial component of a stack of other shot gathers shows energy near 0.001 s that is similar but has reversed polarity relative to (a). (d) The tangential component of a stack of the same gathers as (c) shows Lorentz energy at positions orthogonal to the energy in (c).

Figure 10a shows the amplitude of the Lorentz field event in Figure 9a and b, and Figure 10b shows the amplitude of the Lorentz field event in Figure 9c and d. The amplitude in Figure 10a corresponds with the third of the three lobes of the Lorentz field arrival in Figure 9a (0.0042–0.0065 s, labeled L) whereas the amplitude in Figure 10b was extracted from the second of the three main lobes of the Lorentz event in Figure 9b (0.0025–0.0045 s, also labeled L). Hence, the two amplitude patterns (Figure 10a and b) are in-phase even though the two Lorentz events (Figure 9a and 9c) are 180° out-of-phase. We use equation 1 to model a horizontal dipole at the source point and find our best fit with a dipole oriented ~50° west of north (Figure 10c). This alignment corresponds with the alignment of the cylinder and the person swinging the hammer, not with magnetic north, confirming our interpretation that the horizontal motion **v** of the cylinder and the vertical component of the earth's field **B** are responsible for the Lorentz field. Surprisingly, the horizontal component of **B** coupled to the vertical motion of the aluminum cylinder seems to matter little in the creation of this field.

The Lorentz field is not observed when the metal hammer plate is insulated electrically from the soil or when the soil is sufficiently dry that it acts as an insulator. The Lorentz effect creates an electric current density inside the metal hammer plate. In the case where the plate is in electrical contact with the soil, this current travels into the soil, appears as a quasi-electrostatic current dipole source acting

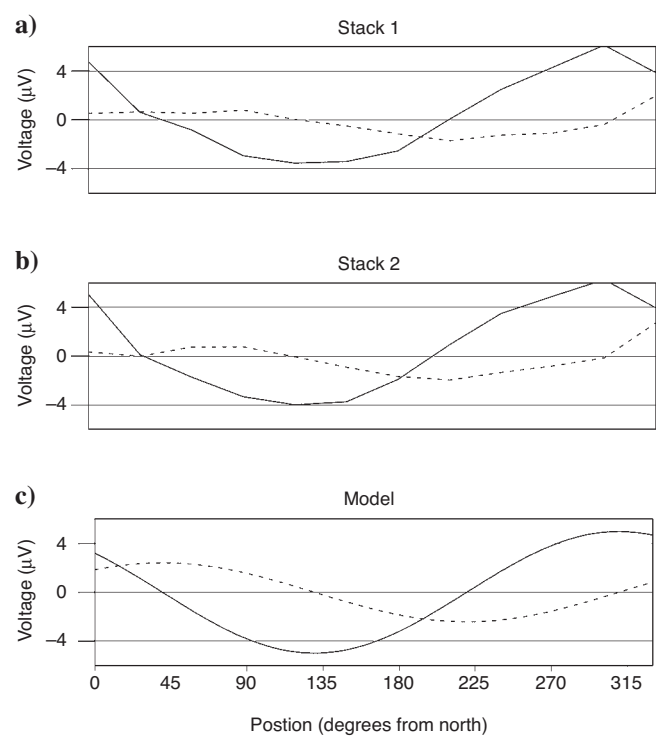

Figure 10. Observed and modeled Lorentz field amplitudes, plotted as a function of radial position (solid = radial, dashed = tangential). (a) Amplitude pattern of arrival marked L in stacks shown in Figure 9a and b. (b) Amplitudes of arrival marked L in stacks shown in Figure 9c and d. (c) Amplitude pattern (theoretical) modeled for a horizontal dipole oriented 50° west of north.

horizontally, and is observed as the Lorentz field. In the case where the plate is insulated from the soil, the current is restricted to the hammer plate and cannot create currents in the soil through conductive effects. Induction is the only way for electric fields to be present in the earth in this case, but induction is vanishingly small across the spatial extent of the study (the EM wavelength associated with these frequencies [$\sim$10–500 Hz] is on the order of kilometers, but the scale of the study is meters). Although the electric field exists in the moving plate in either case (and even in the moving sledgehammer head), it cannot create measureable currents in the earth without electric contact between the moving metal object and the soil. For a more thorough discussion, refer to Haines (2004).

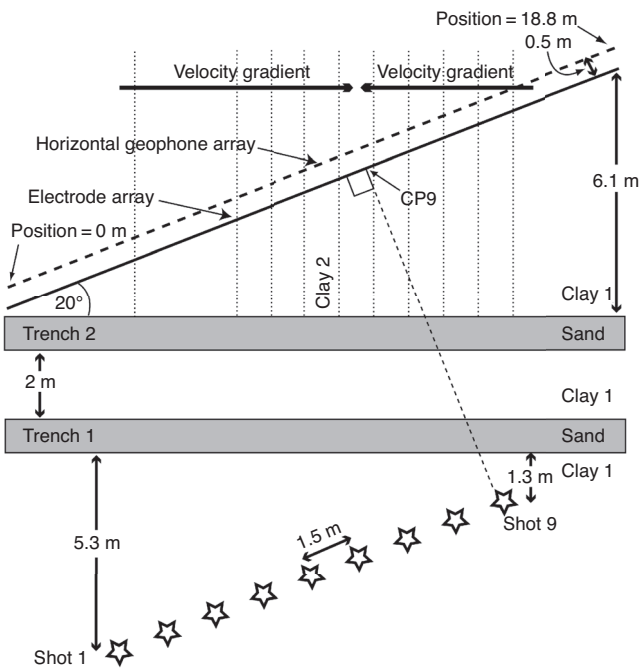

Figure 11. Map schematic of the dipping-trench experimental geometry. CP9 is the point along the receiver line that is closest to shot 9. Dashed lines indicate the boundaries between material blocks used in the finite-difference simulations of the field experiment. Material properties for the blocks are listed in Table 1.

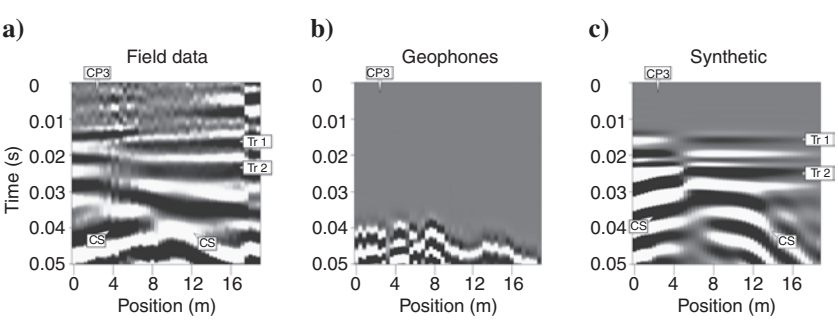

Figure 12. (a) Field seismoelectric, (b) field seismic, and (c) synthetic seismoelectric shot gathers for shot 3. Annotations identify the interface response arrivals for the two trenches (Tr 1 and Tr 2) and the coseismic energy (CS) on the seismoelectric data. The lateral position labeled CP3 is the closest point on the receiver line to the shotpoint (shot 3), marked for reference. The seismic arrivals correspond with the coseismic energy. Data in (a) and (b) are shown after 120–300-Hz band-pass filtering, and the data in (a) are shown with automatic gain control (AGC) (window size is 25 ms).

IMAGING THE TRENCHES

We image the two trenches at the vineyard site using an off-line geometry survey with sources and receivers on opposite sides of the target. This design presents two principal advantages: (1) we record the interface response arrivals from the trenches before the coseismic fields and (2) any source-related fields will not be recorded because the electrodes are sufficiently distant from the source points. A line of explosive sources is parallel to and about 10 m away from the line of electrode receivers (Figure 11). These two lines are at an angle of 20° to the trenches, so we image the trenches as dipping interfaces rather than as flat ones. We also simulate the seismoelectric phenomena using the finite-difference numerical algorithm described by Haines and Pride (2006), providing synthetic data to complement the field data set. Material properties for the 2D (map-view) model were determined by forward modeling and are shown in Figure 11.

Field data and numerical simulations

A line of nine chemical explosive sources at 1.5-m intervals provides our seismic energy (Figure 11). These were 0.3-kg charges except for the shots at positions 3 and 7, which were 0.45 kg. All shots were approximately 1.5 m deep in hand-augered holes that were backfilled and tamped with native material. The shots were detonated with blasting caps fired by a small battery. Each charge provided one seismoelectric shot gather recorded by the receiver array. We simultaneously recorded each shot with a total of 96 channels—48 channels of electrode dipoles and 48 horizontal geophones. The electrode array was composed of 1.4-m dipoles spaced at 0.4-m intervals. The geophone array was composed of 14-Hz Mark Products model L-28 horizontal geophones at 0.4-m intervals, aligned along the direction of the receiver line. Although geophones located within electrode dipoles do not create noticeable electric noise (Haines, 2004), the geophone line was positioned 0.5 m behind the electrode line to avoid any possibility of signal contamination. Data were collected in March, so the soil was nearly saturated at the site.

We used a simple battery-and-blasting-cap firing technique to minimize trigger-related electrical noise, but this approach left the exact shot timing to be determined manually. Comparison with hammer-source data (activated by a trigger switch accurate to $\sim$0.5 ms) provided a basis for setting time zero for the gathers. Fine adjustments of the relative timing between individual shot gathers were made on the basis of first-arrival time on the geophone gathers (geophone and electrical data were recorded simultaneously).

Figure 12a shows the seismoelectric record from shot 3, with annotations identifying the arrivals. Note that the interface response arrival from the first trench (Tr 1) shows higher frequency energy than the interface response arrival from the second trench (Tr 2), caused by seismic attenuation of the higher frequencies while the seismic wave traveled from the first trench to the second. (Absorption of the interface response is negligible, as discussed earlier.) The interface responses from the two sides of each trench interfere to produce only one distinct interface response arrival for each trench because the trench width is small-

er than the seismic wavelength. The coseismic energy (CS) shows different arrival times at different offsets as is expected; however, the moveout is not exactly the hyperbolic shape expected for a fan-profile shot in homogeneous material. In particular, the earliest part of the coseismic first arrival occurs at the receiver position near 10 m rather than near 2 m (the point on the receiver line that is closest to the shotpoint, labeled CP3 in Figure 12). This pattern is also evident in the geophone data (Figure 12b). Thus, velocity heterogeneity clearly exists at our field site, and it causes coseismic energy to arrive earlier than otherwise expected at receivers around the position near 10 m.

Figure 12c shows the synthetic seismoelectric shot gather for shot 3 produced by finite-difference modeling. The geometry of the 2D model space matches the field site (Figure 11), with the nontrench material (clayey soil) extending about 4 m beyond the ends of the trenches for the seismic propagation modeling and approximately 20 m beyond the trenches for the electrical simulation. All blocks are 97% saturated with pore water of pH 7 and salinity 0.001 mol/liter. The seismic velocities are consistent with Gassmann's (1951) equation for partially saturated materials. In our modeling, we have allowed for partial saturation by using a formation factor F given by a modified Archie's law $F = (\phi S)^{-3/2}$ (ϕ is soil porosity and S is water saturation) and by using an effective fluid bulk modulus given by $1/K_f = (1 - S)/K_{\text{air}} + S/K_{\text{water}}$ and an effective fluid density given by $\rho_f = (1 - S)\rho_{\text{air}} + S\rho_{\text{water}}$. The fluid bulk modulus enters into the Gassmann expressions used to model the poroelastic constants (see equations 7–9 of Haines and Pride, 2006), while the formation factor enters into the various transport coefficients of the electrokinetic transport laws (see equations 10–12 of Haines and Pride, 2006). We include the high-velocity body in the numerical modeling as a rectangular region comprising nine strips that provide a gradual transition from the low-velocity clay (Clay 1 in Table 1) to the highest velocity (Clay 2), as shown in Figure 11. We include the high-velocity body in order to reduce misfit between the observed and modeled data. The velocity distribution was determined through seismoelectric forward modeling and was intended to produce synthetic data that capture the basic trends of the field data. The remaining misfit between synthetic and field data results from the simplicity of the block model and imperfect forward modeling. The point source is isotropic and is scaled to represent 0.45 kg of explosive. The source time signature is a 200-Hz Ricker wavelet. The basic patterns of the seismoelectric arrivals in the synthetic gather (Figure 12c) match the field-data gather shown in Figure 12a—interface response events from the two trenches (Tr 1 and Tr 2), followed by the nonhyperbolic coseismic energy (CS). Because the modeling algorithm does not include seismic absorption (other than the minuscule loss caused by the Biot flow), we have applied a time-varying, high-cut filter to the synthetic data to reduce the frequency content of later arrivals (the coseismic fields), improving the similarity of the synthetic data to the field data.

Table 1. Material properties for the blocks in Figure 11.

Material	V_p (m/s)	Porosity (%)	Permeability (m^2)	Conductivity (S/m)
Sand	263	30	10^{-11}	0.01
Clay 1	393	10	10^{-14}	0.05
Clay 2	555	10	10^{-14}	0.05

Figure 13 shows the field and synthetic gathers from shots 1 and 5, and Figure 14 shows the gathers from shots 7 and 9. The general patterns are the same as the gather for shot 3 (Figure 12a and 12c)—flat interface response arrivals from the two trenches followed by the curved coseismic energy. The arrival time of the interface response becomes earlier as the shots approach the trenches (from shot 1 to

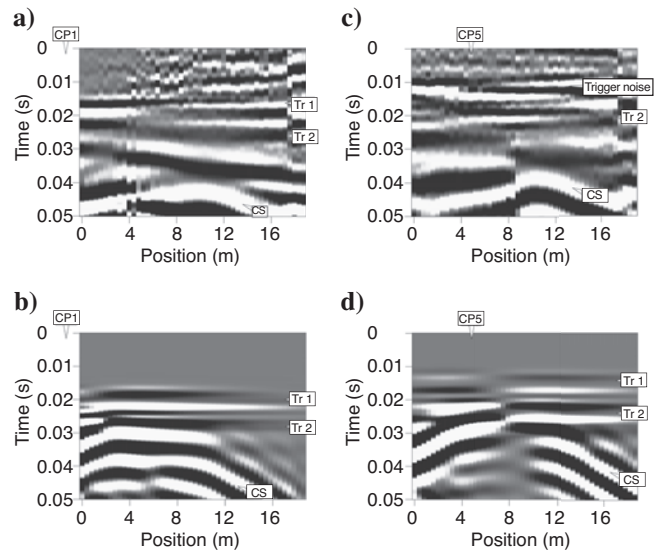

Figure 13. Field (top row) and synthetic (bottom row) seismoelectric shot gathers for shots 1 (top) and 5 (bottom). All field data (a, c) have undergone 60-Hz energy removal and are displayed with a 120–300-Hz bandpass filter and AGC (25-ms window). Interface response arrivals for the two trenches are labeled (Tr 1 and Tr 2), along with coseismic energy (CS). Also labeled are the points on the receiver line that are closest to the shotpoint for each gather, labeled CPx, where x is the shot number.

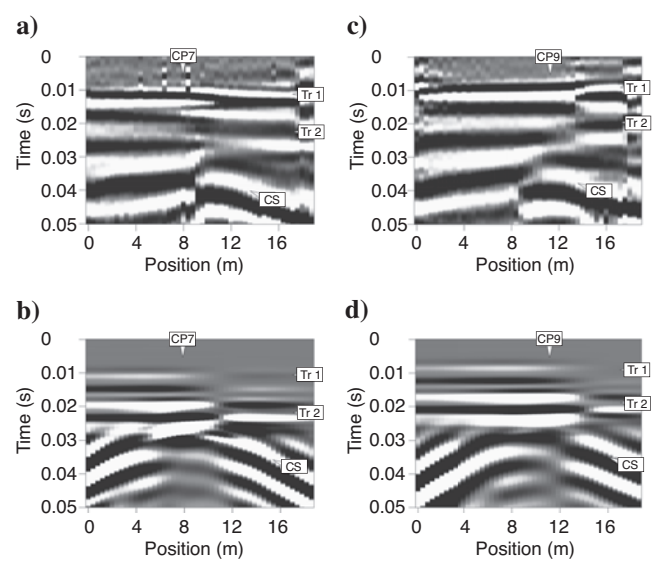

Figure 14. Field (top row) and synthetic (bottom row) seismoelectric shot gathers for shots 7 (a, c) and 9 (b, d). Processing and labels are the same as in Figure 13.

shot 9) because the interface response occurs when the seismic energy reaches the interface. If seismic velocity at the field site were homogeneous, the coseismic arrivals would be hyperbolic (centered at the positions labeled on the data plots as CPx, where x is the shot number) and would arrive at the same time on all shot gathers (because the distance from the shot to the receiver line is the same for all shots). But because the higher-numbered shots are nearer to the high-velocity body, the coseismic arrivals occur earlier for these shots than for those that are more distant from the high-velocity body (the coseismic field for shot 9 is observed earliest in time, and the coseismic field for shot 1 is observed latest).

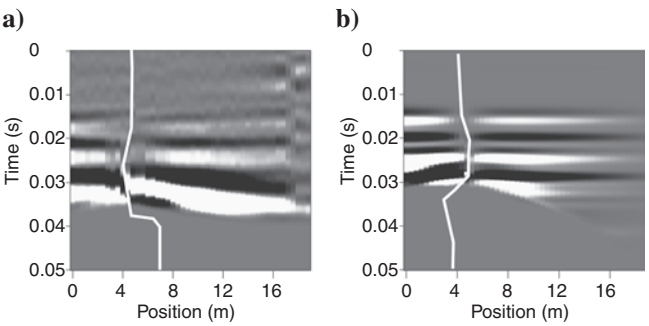

Figure 15. (a) Field and (b) synthetic seismoelectric shot gathers for shot 3 (compare with Figure 12) after polarity flipping. The location of the polarity flip has been manually picked and is indicated by the white line.

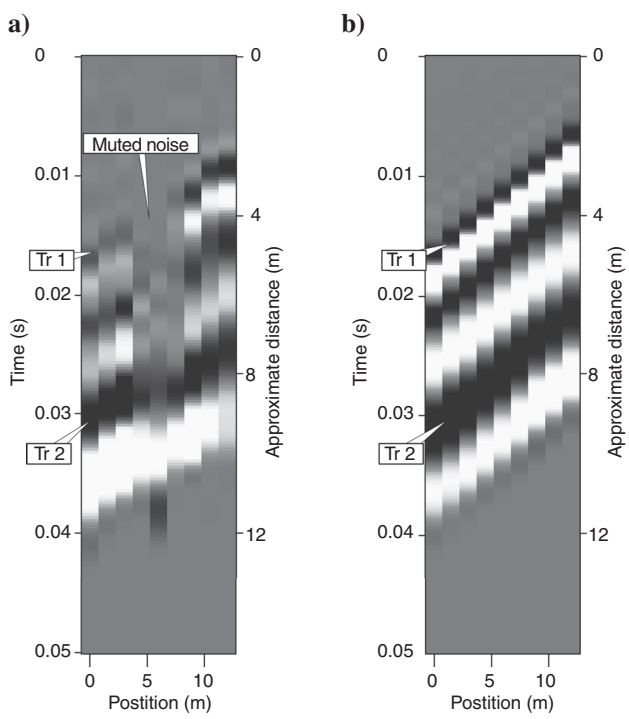

Figure 16. (a) Field and (b) synthetic images of the two trenches, produced by stacking shot gathers after muting the unwanted noise. Each trace is the result of stacking one shot gather after applying mutes. Arrivals are annotated, and an approximate distance scale is noted, based on V_p = 300 m/s.

Note the arrival on the field-data gather for shot 5 (Figure 13c) that is identified as trigger noise. A similar arrival exists in the field data for shot 4 (not shown). These arrivals occur at nearly the time expected for the first trench interface response, but they arrive earlier than expected and do not show the amplitude pattern of the interface response. We interpret these arrivals as the combination of trigger-related noise and the interface response arrival from the first trench. It is unclear why only these two gathers were impacted by this trigger-related energy; perhaps the shot wires were positioned differently than for the other shots and created a measurable electric field. We do not notice an appreciable difference between quality of data from the two sizes of explosive charges that were used.

For all of the field-data gathers except shot 4, we have removed power-line noise (60 Hz and its harmonics) using the frequency revision approach described by Butler and Russell (2003). For shot 4 we find the best results using the sinusoidal subtraction approach described by Butler and Russel (1993). After power-line noise removal, we use a 120–300-Hz band-pass filter to minimize background electrical noise and coseismic fields.

Trench images

Because our trench survey geometry (Figure 11) is more complex than a simple surface survey, the assignment of seismoelectric energy to specific locations is also more complex. The location of the center of each interface response arrival depends on the location of the point on the corresponding interface that is nearest the shotpoint (that is, the location of the first seismic Fresnel zone) and its orientation with respect to the receiver line. As can be clearly seen in the synthetic shot gathers (Figures 12c, 13b and d, and 14b and d), the interface response polarity reversals do not occur at exactly the same point for the two interface response events in each gather, and neither of these polarity reversal points is the same as the center of the coseismic event. We manually pick a broken line for each shot gather around which to reverse the polarity.

We apply a tail mute to all seismoelectric shot gathers to remove the coseismic energy (because of the experimental geometry, we do not expect any interface response arrivals within the coseismic fields), and we flip the polarity of the shot gathers around the line that we picked. Figure 15 shows the muted and polarity-flipped versions of the field and synthetic gathers for shot 3, with the reversal line marked by a thick white line. We process the other shot gathers in a similar manner. Following the example of standard seismic processing techniques, we use front mutes to remove the trigger noise from shot gathers 4 and 5. We stack each shot gather to produce a single trace that corresponds with one region of the subsurface. By placing these traces side by side, we create the images of the two trenches shown in Figure 16a and b (field data and synthetic data, respectively). These images clearly show the two trenches in a dipping geometry.

CONCLUSIONS

We have presented observations of two types of source-related fields that can be observed in seismoelectric data, along with simple analytical representations of them. The Lorentz field is unlikely to prove useful, but can be readily avoided by using a nonmetal hammer plate, or by insulating a metal hammer plate from the soil. The direct field is an electrokinetic effect, and therefore contains information about the shallow subsurface in the immediate vicinity of the source point. Though we have considered it an unwanted field for

our experiments, it is possible that the direct field could be used in geophysical surveys. Perhaps in a downhole setting it could be used to determine information about the flow properties of the area directly adjacent to the borehole. Both of these source-related fields are short-lived and will not be problematic for surveys targeting layers deeper than a few meters (depending on the duration of the fields and the seismic velocity of the material). For inline geometry surface surveys, a trade-off will likely be found between avoiding these source-related fields, and targeting layers so deep that the interface response signal is too weak to record. An optimal depth range will likely be found to vary between sites.

Our field-data trench image is a success in that (1) it clearly shows interface response signals from the two trenches in their correct dipping geometry and (2) it matches the synthetic image to a reasonable degree. Differences between the field and synthetic image are because of velocity heterogeneities beyond those included in our models. A difference in frequency content between the arrivals from the two trenches is clear in the field data and demonstrates that the seismic wave creating the interface response signals has suffered attenuation of the higher frequencies between the first trench and the second. The interface response arrival from the first trench is of higher frequency than the second because the causal seismic wave had higher-frequency content when creating the first interface response than the second. Although the electrodes are nearer to the second trench than to the first, the difference in recording offset for the two interface response events is of no consequence because the wavelength associated with the interface response is orders of magnitude greater than the offsets in our experiments. Because there is no absorption of these fields at our scale of study, the recorded interface response signals have the same frequency content (independent of recording offset) as the seismic waves that created them.

To compensate for the lack of seismic attenuation (other than the negligible loss caused by the Biot flow) in the modeling algorithm, we have applied a time-varying, high-cut filter to the synthetic data, reducing the frequency content of later arrivals. This lack of absorption is one way in which our modeling algorithm differs from reality; the lack of a free surface is another. Although our synthetic shot gathers do not contain surface waves, the final synthetic image would be essentially unchanged if surface waves were included. Because surface waves travel more slowly than P-waves, associated coseismic fields would have been muted with the rest of the coseismic arrivals. Interaction between surface waves and the trenches would have produced some sort of interface response fields; these would interfere with the main interface response arrivals and likely degrade the sharpness of the synthetic image.

Our trench images demonstrate a limitation of the seismoelectric method that it shares with seismic reflection methods. Although the two trenches include four interfaces (one on each side of each trench), the images essentially show only two distinct arrivals. The seismic wavelengths are such that the interface response signals from the two sides of a given trench overlap in time and interfere to produce one broad arrival (as with seismic reflections from a thin layer). The solution to this problem is the same as for seismic reflection: higher-frequency seismic sources would provide separate signals from each side of each trench.

The methods used to create our images demonstrate a data processing difficulty associated with off-line geometry surveys. We manually picked the polarity-reversal points, around which we flipped the polarity of the data before stacking. Trivial for a nine-shot survey, this picking would be time consuming for a larger or more complex survey. An inverse algorithm could use an imaging condition to identify the point of polarity reversal and migrate interface response energy to the correct position in the image. A more sophisticated version could incorporate coseismic fields into the development of an earth model.

We have described experimental methods designed specifically to record the interface response and coseismic fields separately, and we have exploited these methods to isolate and study these seismoelectric fields. With a SNR that can often be on the order of 0.01, coseismic contamination of seismoelectric records is a signal-to-noise separation problem similar to surface-wave contamination of near-surface seismic reflection records. This problem can be approached with data processing methods or by exploiting off-line survey geometries as we did to create our image of the trenches. This second option is not available with reflection seismic techniques or most other geophysical methods; off-line survey geometries use transmitted modes (in this case, seismic-to-electromagnetic conversions). Because we are recording converted phases, we can create reflection-type images using survey geometries that can yield only tomographic-type information with most methods (e.g., P- or S-wave seismic methods, radar, electrical resistivity). For instance, a seismic image created with the same survey geometry as our seismoelectric image would be limited to velocity tomography and likely would not be able to resolve the trenches. This flexibility, inherent in the seismoelectric method, provides a convenient means to avoid recording the coseismic and source-related fields that otherwise present a challenging data processing problem. Crosswell surveys are a particularly promising type of off-line geometry because the seismic sources and electrode receivers could be positioned near to the targets of interest, permitting the use of high-frequency seismic sources and facilitating the recording of weak signals that fall off rapidly with distance because of the nature of the dipole field.

ACKNOWLEDGMENTS

The data presented here would not exist without the efforts of those who swung the hammer: Nick Martin, Jordan Muller, Brian Ebel, Mike Beman, Ashley Griffith, Rob Sanders, Phil Resor, T. J. Kiczenski, Stephan Bergbauer, Antoine Guitton, Morgan Brown, and Jonathan Franklin. Jerry Harris has been an essential source of insight and guidance since the inception of this project. We are very grateful to Jim and Carolyn Pride and to George and Anita Thompson for use of field sites on their property. We offer many thanks to Rufus Catchings and Tom Burdette for help with data collection. Art Thompson graciously provided some essential electronics, along with important input on data collection. Chunling Wu (Stanford Tomography Project) wrote the poroelastic simulation code that calculates the mechanical part of the seismoelectric simulations. Dave Alumbaugh and Adam Pidlisecky provided important insight on electric fields in the earth. Acknowledgment is made to the donors to the American Chemical Society Petroleum Research Fund for support of this research. Additional funding has been provided by the Achievement Rewards for College Scientists Foundation, the Stanford School of Earth Sciences McGee Fund, the AAPG student research grants program, the GSA student research grants program, the Colorado Geological Survey, and the Stanford Exploration Project. This manuscript was significantly improved through the comments of anonymous reviewers and associate editor John Bradford.

REFERENCES

Butler, K., A. Kepic, and M. Rosid, 2002, An experimental seismoelectric survey for groundwater exploration in the Australian Outback: 72nd Annual International Meeting, SEG, Expanded Abstracts, 1484–1487.

Butler, K. E., and R. D. Russell, 1993, Subtraction of powerline harmonics from geophysical records: Geophysics, **58**, 898–903.

———, 2003, Cancellation of multiple harmonic noise series in geophysical records: Geophysics, **68**, 1083–1090.

Butler, K. E., R. D. Russell, A. W. Kepic, and M. Maxwell, 1996, Measurement of the seismoelectric response from a shallow boundary: Geophysics, **61**, 1769–1778.

Garambois, S., and M. Dietrich, 2001, Seismoelectric wave conversions in porous media: Field measurements and transfer function analysis: Geophysics, **66**, 1417–1430.

———, 2002, Full waveform numerical simulations of seismoelectromagnetic wave conversions in fluid-saturated stratified porous media: Journal of Geophysical Research, **107**, 10.1029/2001JB000316.

Gassmann, F., 1951, Über die Elastizität poröser Medien: Vierteljahrsschrift der Naturforschenden Gesellschaft in Zürich, **96**, 1–23.

Haartsen, M. W., and S. R. Pride, 1997, Electroseismic waves from point sources in layered media: Journal of Geophysical Research, **102**, 24745–24769.

Haines, S., 2004, Seismoelectric imaging of shallow targets: Ph.D. dissertation, Stanford University.

———, 2006, Design and application of an electromagnetic vibrator seismic source: Journal of Environmental and Engineering Geophysics, **11**, 9–15.

Haines, S., A. Guitton, B. Biondi, and S. Pride, 2003, Development experimental methods in electroseismics: 73rd Annual International Meeting, SEG, Expanded Abstracts, 560–563.

Haines, S., and S. Pride, 2006, Seismoelectric numerical modeling on a grid: Geophysics, **71**, no. 6, N57–N65.

Haines, S., S. Pride, S. Klemperer, and B. Biondi, 2004, Development of electroseismic experimental methods: Symposium on the Application of Geophysics to Engineering and Environmental Problems, Environmental and Engineering Geophysical Society, Expanded Abstracts, 1490–1503.

Ivanov, A., 1939, Effect of electrization of earth layers by elastic waves passing through them: Doklady Akademii Nauk SSSR, **24**, 41–45.

Landau, L., and E. Lifshitz, 1984, Electrodynamics of continuous media, 2nd ed.: Pergamon Press, Inc..

Martner, S. T., and N. R. Sparks, 1959, The electroseismic effect: Geophysics, **24**, 297–308.

Mikhailov, O. V., M. W. Haartsen, and M. N. Toksoz, 1997, Electroseismic investigation of the shallow subsurface: Field measurements and numerical modeling: Geophysics, **62**, 97–105.

Miller, R. D., S. E. Pullan, D. W. Steeples, and J. A. Hunter, 1992, Field comparison of shallow seismic sources near Chino, California: Geophysics, **57**, 693–709.

———, 1994, Field comparison of shallow P-wave seismic sources near Houston, Texas: Geophysics, **59**, 1713–1728.

Pride, S., 1994, Governing equations for the coupled electromagnetics and acoustics of porous media: Physical Review B, **50**, 15678–15696.

Pride, S. R., and M. W. Haartsen, 1996, Electroseismic wave properties: Journal of the Acoustical Society of America, **100**, 1301–1315.

Shaw, D., 1992, Introduction to colloid and surface chemistry, 4th ed.: Butterworths.

Thompson, A. H., and G. A. Gist, 1993, Geophysical applications of electrokinetic conversion: The Leading Edge, **12**, 1169–1173.

Thompson, A. H., S. Hornbostel, J. Burns, T. Murray, R. Raschke, J. Wride, P. McCammon, J. Sumner, G. Haake, M. Bixby, W. Ross, B. White, M. Zhao, and P. Pecsak, 2005, Field tests of electroseismic hydrocarbon detection: 75th Annual International Meeting, SEG, Expanded Abstracts, 565–568.

Zhu, Z., M. W. Haartsen, and M. N. Toksoz, 2000, Experimental studies of seismoelectric conversions in fluid-saturated porous media: Journal of Geophysical Research, **105**, 28055–28064.